

Theoretical and Experimental Investigation of a 60 GHz Off-Body Propagation Model

Theodoros Mavridis, Luca Petrillo, Julien Sarrazin, David Lautru, Aziz Benlarbi-Delaï, and Philippe De Doncker

Abstract—A fast computation and accurate analytical model for off-body propagation is derived in this paper. The paper discusses the off-body model propagation from an external source to a receiver located on the body. The model is developed for normal incident plane wave by describing the human body with a circular cylinder. We show that the total received electric field around the human body can be written as a creeping wave in the shadow region and as a Geometrical Optics result for the lit region. It is also shown that at 60 GHz, the shadow boundary width is negligible. The model shows perfect agreement with the experimental results conducted on a perfectly conducting cylinder. Measurements of the creeping wave path gain have been also conducted on a real body to assess the validity of the cylinder assumption. The results have shown a path gain of about 5 dB/cm for TM case and 3 dB/cm for TE case. The standard deviation between the measurements and the cylindrical model is about 3.5 dB for both TM and TE cases.

Index Terms—off-body, BAN, creeping wave, millimeter wave, 60 GHz, V-band, human body, propagation, channel modelling

I. INTRODUCTION

The popularity of wireless communication technologies has increased the need for reliable, high-speed communications. To cope with the need for high-data rate transmission, successive technologies have been proposed that use large bands of the RF spectrum. The next emerging technology to realize short-range indoor communication with data rates of a few Gbit/s seems to be the 60 GHz systems [8]. The progress in low-cost mm-wave circuit design and the wide available spectrum around 60 GHz will allow to develop new communication services such as HD streaming video, augmented reality, wireless gaming, Gigabit Ethernet,... [25]. Within this framework, the development of 60 GHz Body Area Networks (BANs) (off- and on-body) [2], [4] is important.

The propagation paths between body-mounted antennas have been widely studied at lower frequencies such as 2.45 GHz [6], [10], [21] or in Ultra Wideband between 3.1 and 10.6 GHz [5], [7], [24]. Measurements but also finite difference time domain (FDTD) simulations [26] have described the BAN communication channel.

At higher frequency such as 60 GHz, human body influence has been studied in order to model shadowing [9], [13]. But in

the BAN context, the fields have to be computed in the close vicinity of the human body, which has not yet been done.

Narrowband and UWB indoor measurements [16], [17] have lead to the 60 GHz standardized IEEE 802.11ad [18] channel model. In the standard, the channel model generation is made of two steps. The first one is to simulate by ray tracing the main propagation paths. Then, measurements define the statistics of the intra-cluster paths. The development of a 60 GHz off-body propagation model has to be compatible with this IEEE standard channel model.

This paper focuses on the propagation from an external transmitter to a receiver located on the body assuming that it can be described by a circular cylinder. We propose here to use the results of Uniform Theory of Diffraction (UTD) [20], [22], which is a ray description of the total fields, to develop such a model. The important property of UTD is the spatial continuity of the solution regardless the position around the cylinder, but it necessitates the heavy calculation of Fock functions [20]. In this paper, it is shown that this calculation is not required at 60 GHz to get an accurate solution of the scattering by a convex cylinder describing the human body. Under the millimeter wavelength hypothesis, a new model extending our previous work [19] based on a simplification of UTD is proposed. Compared to the previous work limited to conducting cylinders, the new model can predict the electric field around a real human body at 60 GHz for a normal incident plane wave. The total fields can be split into only two spatial (lit and shadow) solutions which are not necessary continuous. The solutions for the lit and shadow regions are derived from Geometrical Optics (GO) and the creeping wave formulation. This model have been validated by measurements on a real human body, which confirm the assumption that it can be modeled by a circular cylinder at 60 GHz. Those solutions are well suited for being included in a standard such as IEEE 802.11ad. The main contributions of this paper are a ready-to-use propagation model for an off-body scenario and the validation of the circular geometry for the human body at 60 GHz.

Section II presents the general equations of a plane wave diffracted by a circular cylinder and develops our model. Both TM and TE polarizations are considered in the dielectric and perfectly conducting cases. Section III validates our model by numerical comparisons of the different approaches. The comparison between our model and the boundary value problem solution [3] shows perfect agreement. Section IV proposes the experimental set-up and compares the model to the experimental results for both polarizations. The measurements have been done on a metallic cylinder and on a real body. Finally, Section

T. Mavridis, L. Petrillo and P. De Doncker are with OPERA Dpt. - Wireless Communications Group, Université Libre de Bruxelles (ULB), B-1050 Brussels, Belgium e-mail: (tmavridi@ulb.ac.be ; lpetrillo@ulb.ac.be ; pdedonck@ulb.ac.be)

J. Sarrazin, D. Lautru and A. Benlarbi-Delaï are with L2E Dept., Université Pierre et Marie Curie (UPMC), F-75005 Paris, France e-mail: (julien.sarrazin@upmc.fr; david.lautru@upmc.fr; aziz.benlarbi_delai@upmc.fr)

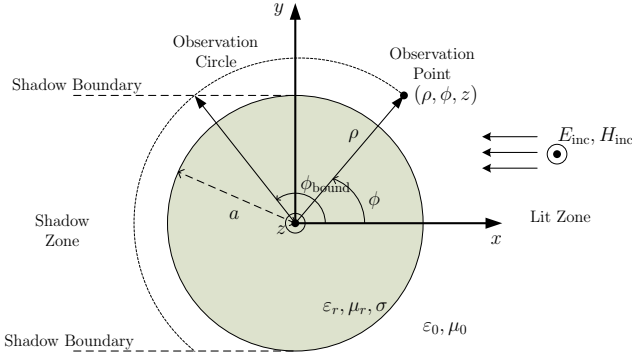


Fig. 1. Problem geometry. The incident electric field \mathbf{E}_{inc} is along \hat{z} for TM polarization and the incident magnetic field \mathbf{H}_{inc} is along \hat{z} for TE polarization. The shadow boundary divides space into two zones: lit and shadow.

V concludes this paper.

II. DIFFRACTED WAVE EQUATIONS

A. Problem Definition

The geometry under study for off-body communication modeling is shown in Fig. 1.

The cylinder modeling the body is immersed in free-space. The cylinder has a radius a , a principal axis \hat{z} , relative permeability μ_r and relative complex permittivity ε_r depending on the conductivity σ by $\varepsilon_r = \varepsilon_r' + \frac{\sigma}{j\omega\varepsilon_0}$ with ε_r' defined as the real part of the relative permittivity and ε_0, μ_0 are respectively the free-space permittivity and permeability. A time dependence $e^{j\omega t}$ is assumed and suppressed, where $\omega = 2\pi f$ is the angular frequency and f is the frequency. Cylindrical coordinates (ρ, ϕ, z) are adopted where $-\pi \leq \phi \leq \pi$, $\rho > a$ and $-\infty \leq z \leq \infty$. In the following, the solution will be studied for positive values of ϕ . By symmetry, the conclusions are exactly the same for negative values of ϕ .

The incident electric field \mathbf{E}_{inc} for TM polarization is defined by:

$$\mathbf{E}_{\text{inc}} = E_0 e^{jk_0 x} \hat{z} \quad (1)$$

where E_0 is the electric field amplitude, $k_0 = \omega/c$ is the free-space wavenumber and c is the speed of light. The magnetic field \mathbf{H}_{inc} for TE polarization is defined as:

$$\mathbf{H}_{\text{inc}} = H_0 e^{jk_0 x} \hat{z} \quad (2)$$

where H_0 is the magnetic field amplitude. Geometrically (see Fig. 1.), the shadow boundary separating the lit and the shadow regions is defined by:

$$\phi_{\text{bound}} = \frac{\pi}{2} + \cos^{-1}\left(\frac{a}{\rho}\right) \quad (3)$$

As can be observed in Fig. 1., the lit region is defined by $\phi < \phi_{\text{bound}}$ and the shadow region by $\phi > \phi_{\text{bound}}$.

B. Dielectric Cylinder Solution

1) *Lit region:* The behaviour of the electric field in the lit region is given by geometrical optics (GO) which defines the electric field as the sum of two waves : the incident and reflected one. GO [14] defines the reflection coefficient \bar{R} for the electric field \mathbf{E} . The reflection coefficient depends on the electric properties of the cylinder and the interface curvature. The total field is then expressed as :

$$\mathbf{E}_{\text{tot}} = \mathbf{E}_{\text{inc}} + \bar{R} \mathbf{E}_{\text{refl}} \quad (4)$$

which takes into account the media losses and the geometry [14]. Equation (4) is not detailed for the dielectric cylinder case although it is developed in sections II-C and II-D for the PEC cylinder case.

2) Shadow region:

a) *TM polarization:* The total field around the cylinder is given by [3]:

$$E_z^{\text{TM}} = E_0 \sum_{n=-\infty}^{\infty} j^n \{J_n(k_0 \rho) + a_n H_n^{(2)}(k_0 \rho)\} e^{-jn\phi} \quad (5)$$

with

$$a_n = \frac{J_n'(k_0 a) J_n(k_1 a) - \sqrt{\varepsilon_r / \mu_r} J_n(k_0 a) J_n'(k_1 a)}{\sqrt{\varepsilon_r / \mu_r} J_n'(k_1 a) H_n^{(2)}(k_0 a) - J_n(k_1 a) H_n^{(2)'}(k_0 a)} \quad (6)$$

where $k_1 = k_0 \sqrt{\varepsilon_r \mu_r}$ is the wavenumber inside the cylinder. Functions J_n and $H_n^{(2)}$ are respectively the first kind Bessel functions and the second order Hankel functions defined in [1]. In following equations, E_0 is normalized to unity. It can be shown that (6) can be written in the high frequency range [22] as:

$$a_n = -\frac{J_n'(ka) - Q J_n(ka)}{H_n^{(2)'}(ka) - Q H_n^{(2)}(ka)} \quad (7)$$

where $Q = j\eta$, $\eta = \sqrt{\varepsilon_r / \mu_r}$ is the normalized admittance with respect to the free space admittance $\sqrt{\varepsilon_0 / \mu_0}$ [15] and $k = k_0$.

At high frequencies, (5) converges slowly due to the oscillations of the Bessel functions with large argument. To speed up convergence, it is necessary to introduce Uniform Theory of Diffraction (UTD) results [20]. Watson's transformation [23] allows to obtain a solution with faster convergence by using the theorem of residue:

$$E_z^{\text{TM}} = 2\pi \sum_s j^{\tilde{v}_s} \frac{J_{\tilde{v}_s}'(ka) - Q J_{\tilde{v}_s}(ka)}{H_{\tilde{v}_s}^{(2)''}(ka) - Q H_{\tilde{v}_s}^{(2)'}(ka)} H_{\tilde{v}_s}^{(2)}(k\rho) \Phi_{\tilde{v}_s}(\phi) \quad (8)$$

where:

$$\Phi_{\tilde{v}_s}(\phi) = \frac{\cos(\tilde{v}_s(\phi - \pi))}{\sin(\tilde{v}_s \pi)} \quad (9)$$

with \tilde{v}_s verifying:

$$H_{\tilde{v}_s}^{(2)'}(ka) - Q H_{\tilde{v}_s}^{(2)}(ka) = 0 \quad (10)$$

Calculation of Bessel functions of complex order is not trivial. It is proposed to introduce $A(z)$, the first kind Airy's functions [1] and $W_2(z) = 2e^{j\pi/6} \sqrt{\pi} A(e^{j4\pi/3} z)$, the second kind [12].

By defining $h = k(\rho - a)/m$ and $m = (ka/2)^{1/3}$, (8) can be approximated, when $\rho \simeq a$, by:

$$E_{\text{Shadow}}^{\text{TM}} \simeq 2\pi \sum_s j^{\tilde{v}_s} \frac{A'(\tilde{\tau}_s) - qA(\tilde{\tau}_s)}{\tilde{\tau}_s W_2(\tilde{\tau}_s) - qW_2'(\tilde{\tau}_s)} W_2(\tilde{\tau}_s - h) \Phi_{\tilde{v}_s}(\phi) \quad (11)$$

In (11), $q = mQ$, $\tilde{\tau}_s$ is defined by $\tilde{v}_s = ka + m\tilde{\tau}_s$ and $\tilde{\tau}_s$ verifies:

$$W_2'(\tilde{\tau}_s) - qW_2(\tilde{\tau}_s) = 0 \quad (12)$$

which simplifies equation (10). In (11), the first term of the sum gives the asymptotic behaviour of the electric field. The higher order terms ($s \geq 2$) increase the accuracy around the shadow boundary. Noting that, around 60 GHz, $|\text{Im}(\tilde{v}_1)| \ll |\text{Im}(\tilde{v}_s)|$ with $s > 2$ ($\text{Im}(x)$ is the imaginary part of x), (11) can be approximated by :

$$E_{\text{Shadow}}^{\text{TM}} \simeq 2\pi j^{\tilde{v}_1+1} \frac{A'(\tilde{\tau}_1) - qA(\tilde{\tau}_1)}{\tilde{\tau}_1 W_2(\tilde{\tau}_1) - qW_2'(\tilde{\tau}_1)} W_2(\tilde{\tau}_1 - h) e^{-j\tilde{v}_1\phi} \quad (13)$$

by making the approximation $\Phi_{\tilde{v}_s}(\phi) \simeq j e^{-j\tilde{v}_s\phi}$ which is equivalent to keep the creeping wave mode coming from the $\phi > 0$ and neglecting the wave coming from the other side ($\phi < 0$). Equation (13) finally gives the creeping wave around a dielectric cylinder for a TM incident wave. By defining the path gain $P = 20 \log(\frac{|E_z|}{1\text{V/m}})$ in [dBV/m] :

$$P_{\text{shadow}}^{\text{TM}} = 20 \log \left| 2\pi \frac{A'(\tilde{\tau}_1) - qA(\tilde{\tau}_1)}{\tilde{\tau}_1 W_2(\tilde{\tau}_1) - qW_2'(\tilde{\tau}_1)} W_2(\tilde{\tau}_1 - h) \right| + 20 \log(e)m|\text{Im}(\tilde{\tau}_1)|(\pi/2 - \phi) \quad (14)$$

by using the fact that $|j^{\tilde{v}_1+1} e^{-j\tilde{v}_1\phi}| = |e^{j\tilde{v}_1(\pi/2-\phi)}| = |e^{jk a(\pi/2-\phi)} e^{jm\tilde{\tau}_1(\pi/2-\phi)}| = |e^{jm\tilde{\tau}_1(\pi/2-\phi)}|$. A simplified path gain writing can be inferred from (14):

$$P_{\text{shadow}}^{\text{TM}} = P_{\pi/2}^{\text{TM}} + n_{\text{dielec}}^{\text{TM}}(\pi/2 - \phi) \quad (15)$$

by defining the gain factor $n_{\text{dielec}}^{\text{TM}} = 20 \log(e)m|\text{Im}(\tilde{\tau}_1)|$ and the received power at $\pi/2$: $P_{\pi/2}^{\text{TM}}$. It can be equivalently written in terms of ϕ_{bound} :

$$P_{\text{shadow}}^{\text{TM}} = P_{\text{bound}}^{\text{TM}} + n_{\text{dielec}}^{\text{TM}}(\phi_{\text{bound}} - \phi) \quad (16)$$

where $P_{\text{bound}}^{\text{TM}}$ is the received power at the shadow boundary ϕ_{bound} .

b) *TE polarization*: The total electric field is given by [3] :

$$E_{\rho}^{\text{TE}} = \frac{H_0}{j\omega\varepsilon} \frac{1}{\rho} \times \sum_{n=-\infty}^{+\infty} n j^{n-1} \{J_n(k\rho) + b_n H_n^{(2)}(k\rho)\} e^{-jn\phi} \quad (17)$$

$$E_{\phi}^{\text{TE}} = -\frac{kH_0}{j\omega\varepsilon} \times \sum_{n=-\infty}^{+\infty} j^n \{J_n'(k\rho) + b_n H_n^{(2)'}(k\rho)\} e^{-jn\phi}$$

where the boundary conditions give:

$$b_n = -\frac{QJ_n'(ka) - J_n(ka)}{QH_n^{(2)'}(ka) - H_n^{(2)}(ka)} \quad (18)$$

Again, by applying Watson's transformation, the TE polarization creeping wave modes can be inferred :

$$E_{\rho}^{\text{TE}} = \frac{H_0}{j\omega\varepsilon} \frac{1}{\rho} \times \sum_s \tilde{v}'_s j^{\tilde{v}'_s-1} \frac{QJ_{\tilde{v}'_s}'(ka) - J_{\tilde{v}'_s}(ka)}{QH_{\tilde{v}'_s}^{(2)'}(ka) - H_{\tilde{v}'_s}^{(2)}(ka)} H_{\tilde{v}'_s}^{(2)}(k\rho) \Phi_{\tilde{v}'_s}(\phi) \quad (19)$$

$$E_{\phi}^{\text{TE}} = -\frac{kH_0}{j\omega\varepsilon} \times \sum_s j^{\tilde{v}'_s} \frac{QJ_{\tilde{v}'_s}'(ka) - J_{\tilde{v}'_s}(ka)}{QH_{\tilde{v}'_s}^{(2)'}(ka) - H_{\tilde{v}'_s}^{(2)}(ka)} H_{\tilde{v}'_s}^{(2)'}(k\rho) \Phi_{\tilde{v}'_s}(\phi)$$

The same substitution by Airy's function can be made and the first creeping mode is kept to obtain:

$$E_{\rho}^{\text{TE}} \simeq \frac{H_0}{j\omega\varepsilon} \frac{1}{\rho} 2\pi \tilde{v}'_1 j^{\tilde{v}'_1} \times \frac{qA'(\tilde{\tau}'_1) - A(\tilde{\tau}'_1)}{q\tilde{\tau}'_1 W_2(\tilde{\tau}'_1) - W_2'(\tilde{\tau}'_1)} W_2(\tilde{\tau}'_1 - h) e^{-j\tilde{v}'_1\phi} \quad (20)$$

$$E_{\phi}^{\text{TE}} \simeq \frac{kH_0}{j\omega\varepsilon} \frac{2\pi}{m} j^{\tilde{v}'_1+1} \times \frac{qA'(\tilde{\tau}'_1) - A(\tilde{\tau}'_1)}{q\tilde{\tau}'_1 W_2(\tilde{\tau}'_1) - W_2'(\tilde{\tau}'_1)} W_2'(\tilde{\tau}'_1 - h) e^{-j\tilde{v}'_1\phi}$$

where $\tilde{v}'_s = ka + m\tilde{\tau}'_s$ and $\tilde{\tau}'_s$ are solutions of:

$$qW_2'(\tilde{\tau}'_s) - W_2(\tilde{\tau}'_s) = 0 \quad (21)$$

Equation (20) gives the creeping wave on a dielectric cylinder for a TE incident wave. Defining the path gain $P = 20 \log(\frac{|\sqrt{E_{\phi}^2 + E_{\rho}^2}|}{1\text{V/m}})$ in [dBV/m], as previously, the following expression can be obtained:

$$P_{\text{shadow}}^{\text{TE}} = P_{\text{bound}}^{\text{TE}} + n_{\text{dielec}}^{\text{TE}}(\phi_{\text{bound}} - \phi) \quad (22)$$

where $n_{\text{dielec}}^{\text{TE}} = 20 \log(e)m|\text{Im}(\tilde{\tau}'_1)|$ is the TE gain factor and $P_{\text{bound}}^{\text{TE}}$ is the received power at the shadow boundary $\phi = \phi_{\text{bound}}$.

C. PEC cylinder: TM polarization

The electric field can be derived from (5) with E_0 normalized to unity:

$$E_z^{\text{TM}} = \sum_{n=-\infty}^{\infty} j^n \{J_n(k\rho) - \frac{J_n(ka)}{H_n^{(2)}(ka)} H_n^{(2)}(k\rho)\} e^{-jn\phi} \quad (23)$$

1) *Lit zone*: The expression of the electric field is given by Geometrical Optics (GO) which is an excellent approximation at high frequency. The electric field is obtained by the sum of the direct and reflected waves by writing (4) as done in [14]:

$$E_{\text{Lit}}^{\text{TM}} = e^{jk\rho \cos(\phi)} - e^{jka \cos(\alpha)} \sqrt{\frac{\rho_r}{\rho_r + s_r}} e^{-jks_r} \quad (24)$$

where $\rho_r = \frac{a}{2} \cos \alpha$ and s_r is the distance between the reflection position and the observation position.

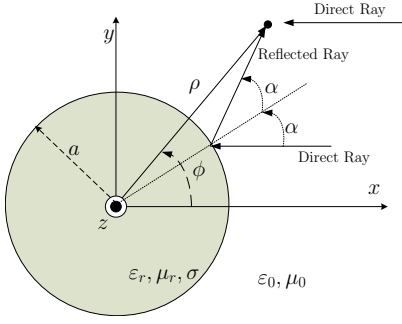


Fig. 2. GO schema for reflected ray

2) Shadow Zone:

$$E_{\text{Shadow}}^{\text{TM}} = 2\pi \sum_s j^{v_s} \frac{A(\tau_s)}{W_2'(\tau_s)} W_2(\tau_s - h) \Phi_{v_s}(\phi) \quad (25)$$

where $v_s = ka + m\tau_s$ and τ_s verifies:

$$W_2(\tau_s) = 0 \quad (26)$$

The τ_s are known and can be written as $\tau_s = -(1.5 q_s)^{2/3} e^{-j\pi/3}$. It has been shown in [12] that q_s can be tabulated as:

$$q_s = \frac{\pi}{4}n + \frac{0.08841941}{n} - \frac{0.083283}{n^3} + \frac{0.4065}{n^5} - \frac{4.91}{n^7} \quad (27)$$

where $n = 4s - 1$ and s is a positive integer.

By keeping the first term, (25) can be approximated by :

$$\begin{aligned} E_{\text{Shadow}}^{\text{TM}} &\simeq 2\pi j^{v_1} \frac{A(\tau_1)}{W_2'(\tau_1)} W_2(\tau_1 - h) \Phi_{v_1}(\phi) \\ &\simeq 2\pi j^{v_1+1} \frac{A(\tau_1)}{W_2'(\tau_1)} W_2(\tau_1 - h) e^{-jv_1\phi} \end{aligned} \quad (28)$$

The path gain expression (16) can be simplified for the PEC case by noting that the first zero of the Airy's function is $\tau_1 = 1.1691 - 2.0249j$:

$$P_{\text{Shadow}}^{\text{TM}} \simeq a_1 + 20 \log |E_0 W_2(\tau_1 - h)| + a_2 m(\pi/2 - \phi) \quad (29)$$

where $a_1 = 0.14985$ and $a_2 = 20 \log(e) \times 2.0249 = 17.588$. The amplitude E_0 of the incident plane wave has been here reintroduced. It can be observed that the attenuation slope only depends on ka via the m factor. Equation (29) is valid for a PEC cylinder for any value of k and a but it is a more accurate solution for large values of ka . By linearity and introducing ϕ_{bound} , the path gain P can be written as :

$$P = P_{\text{bound}}^{\text{TM}} + n_{\text{PEC}}^{\text{TM}}(\phi_{\text{bound}} - \phi) \quad (30)$$

where $n_{\text{PEC}}^{\text{TM}} = a_2 m$ dB/rad.

D. PEC cylinder: TE polarization

In the case of a PEC cylinder, (17) are simplified as :

$$\begin{aligned} E_{\rho}^{\text{TE}} &= \frac{H_0}{j\omega\epsilon} \frac{1}{\rho} \times \\ &\sum_{n=-\infty}^{+\infty} n j^{n-1} \left\{ J_n(k\rho) - \frac{J_n'(ka)}{H_n^{(2)'}(ka)} H_n^{(2)}(k\rho) \right\} e^{-jn\phi} \\ E_{\phi}^{\text{TE}} &= -\frac{kH_0}{j\omega\epsilon} \times \\ &\sum_{n=-\infty}^{+\infty} j^n \left\{ J_n'(k\rho) - \frac{J_n'(ka)}{H_n^{(2)'}(ka)} H_n^{(2)'}(k\rho) \right\} e^{-jn\phi} \end{aligned} \quad (31)$$

1) *Lit Zone*: The magnetic field is given by:

$$H_z^{\text{TE}} = H_0 \left\{ e^{jk\rho \cos(\phi)} + e^{jka \cos(\alpha)} \sqrt{\frac{\rho_r}{\rho_r + s_r}} e^{-jks_r} \right\} \quad (32)$$

Maxwell equations are used to obtain the electric field :

$$E_{\rho}^{\text{TE}} = \frac{1}{j\omega\epsilon} \frac{1}{\rho} \frac{\partial H_z^{\text{TE}}}{\partial \phi} \quad (33)$$

$$E_{\phi}^{\text{TE}} = -\frac{1}{j\omega\epsilon} \frac{\partial H_z^{\text{TE}}}{\partial \rho} \quad (34)$$

2) *Shadow Zone*: The development used in this part is similar to the one used in section II-C. The equations of the TE mode creeping wave are given by :

$$\begin{aligned} E_{\rho}^{\text{TE}} &= \frac{H_0}{j\omega\epsilon} \frac{1}{\rho} \times \\ &2\pi \sum_s v_s' j^{v_s'-1} \frac{A'(\tau_s')}{\tau_s' W_2(\tau_s')} W_2(\tau_s' - h) \Phi_{v_s'}(\phi) \\ E_{\phi}^{\text{TE}} &= -\frac{kH_0}{j\omega\epsilon} \times \\ &\frac{2\pi}{m} \sum_s j^{v_s'} \frac{A'(\tau_s')}{\tau_s' W_2(\tau_s')} W_2'(\tau_s' - h) \Phi_{v_s'}(\phi) \end{aligned} \quad (35)$$

where $v_s' = ka + m\tau_s'$ and τ_s' verifies:

$$W_2'(\tau_s') = 0 \quad (36)$$

The zeroes τ_s' are precisely known and by writing $\tau_s' = -(1.5 q_s')^{2/3} e^{-i\pi/3}$, it can be shown that q_s' can be tabulated as [12]:

$$q_s' = \frac{\pi}{4}l - \frac{0.12378718}{l} + \frac{0.077576}{l^3} - \frac{0.3890}{l^5} + \frac{4.79}{l^7} \quad (37)$$

where $l = 4s - 3$ and s is a positive integer. The first term of sum (35) gives:

$$\begin{aligned} E_{\rho}^{\text{TE}} &\simeq \frac{H_0}{j\omega\epsilon} \frac{1}{\rho} 2\pi v_1' j^{v_1'} \frac{A'(\tau_1')}{\tau_1' W_2(\tau_1')} W_2(\tau_1' - h) e^{-jv_1'\phi} \\ E_{\phi}^{\text{TE}} &\simeq -\frac{kH_0}{j\omega\epsilon} \frac{2\pi}{m} j^{v_1'+1} \frac{A'(\tau_1')}{\tau_1' W_2(\tau_1')} W_2'(\tau_1' - h) e^{-jv_1'\phi} \end{aligned} \quad (38)$$

Knowing $\tau_1' = 0.5094 - 0.8823j$, the path gain (22) can be written as :

$$\begin{aligned} P_{\text{Shadow}}^{\text{TE}} &\simeq a_1' + a_2' m(\pi/2 - \phi) + \\ &20 \log \left| \frac{H_0}{f\epsilon_0} \sqrt{\frac{v_1'^2}{\rho^2} W_2(\tau_1' - h) - \frac{k^2}{m^2} W_2'(\tau_1' - h)} \right| \end{aligned} \quad (39)$$

TABLE I
GAIN FACTORS

a [m]	$n_{\text{skin}}^{\text{TM}}$ [dB/cm]	$n_{\text{PEC}}^{\text{TM}}$ [dB/cm]	$n_{\text{skin}}^{\text{TE}}$ [dB/cm]	$n_{\text{PEC}}^{\text{TE}}$ [dB/cm]
0.15	5.196	5.336	3.397	2.325
0.2	4.300	4.405	2.912	1.919
0.25	3.712	3.796	2.584	1.654
0.3	3.291	3.362	2.343	1.465

where $a'_1 = -11.13965$ and $a'_2 = 20 \log(e) \times 0.8823 = 7.664$. Equation (39) is valid for a PEC cylinder for any value of k and a but it is a more accurate solution for large values of ka . The path gain P is given by:

$$P = P_{\text{bound}}^{\text{TE}} + n_{\text{PEC}}^{\text{TE}}(\phi_{\text{bound}} - \phi) \quad (40)$$

where $n_{\text{PEC}}^{\text{TE}} = a'_2 m$ dB/rad.

III. NUMERICAL SIMULATIONS

The path gain factors at 60 GHz from section II are presented in Table I for different values of the cylinder radius a . The dielectric properties of the human skin at 60 GHz are $\epsilon'_r = 7.9753$ and $\sigma = 36.397$ S/m [11]. For sake of clarity, the path gain factors are expressed in dB/cm.

The validity of the model developed in this paper and the decomposition into two regions (lit and shadow) is first compared for the TM mode. The exact solutions (23) for a PEC cylinder and (5) for a dielectric cylinder are shown in Fig. 3 and in Fig. 4. In the following simulations, the incident electric field magnitude has been normalized to one.

In Fig. 3, it can be observed that the model is very accurate. The exact solution (23) needs about eight hundred terms to converge while the creeping wave solution (25) only needs one term.

The same conclusion can be drawn with Fig. 4 where the model is compared with the exact solution (5) for a cylinder

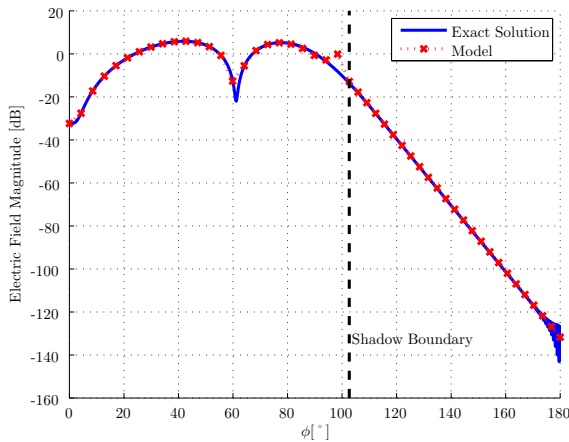


Fig. 3. TM mode. Comparison between the exact solution eq. (23) and the model eq. (24) and (25) for a PEC cylinder with $f = 60$ GHz, $a = 0.2$ m and $\rho = 0.205$ m.

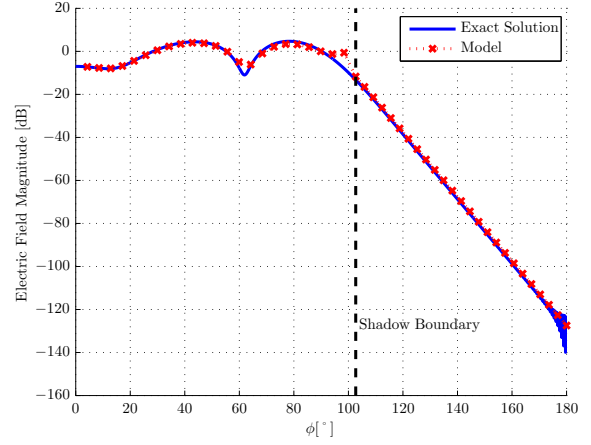


Fig. 4. TM mode. Comparison between the exact solution with a dielectric cylinder eq. (5) and the model with $f = 60$ GHz, $a = 0.2$ m and $\rho = 0.205$ m.

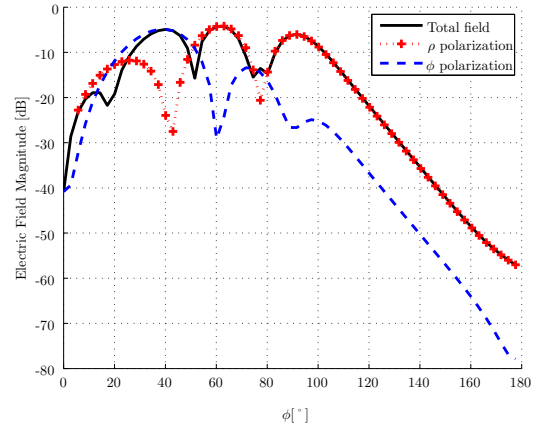


Fig. 5. TE mode. Comparison between the ρ and ϕ polarizations solution with a PEC cylinder with $f = 60$ GHz, $a = 0.2$ m and $\rho = 0.205$ m. The results are plotted using the exact solution.

filled with the dielectric properties of skin at 60 GHz. It can be observed that the accuracy of the GO modeling decreases around the shadow boundary. It can also be observed in Table I, for TM polarization, that the PEC cylinder is a good approximation of a homogeneous cylinder phantom with electrical properties of human skin.

The TE mode can be split into in two components: ρ and ϕ . As can be observed in Fig. 5, the ϕ component of the creeping wave is negligible in the shadow zone.

The dielectric (17) and PEC (18) cylinders are also compared for TE polarization in Fig. 6.

As seen in Fig. 6, the PEC cylinder approximation of the human skin electrical properties filled cylinder is not suitable for the TE case. Fig. 3, 4 and 6 show an interference pattern in the lit region as expected [14]. The valleys and the peaks come from a destructive and constructive interference between the direct ray and the reflected ray.

In the shadow region, the path gain approximation shows

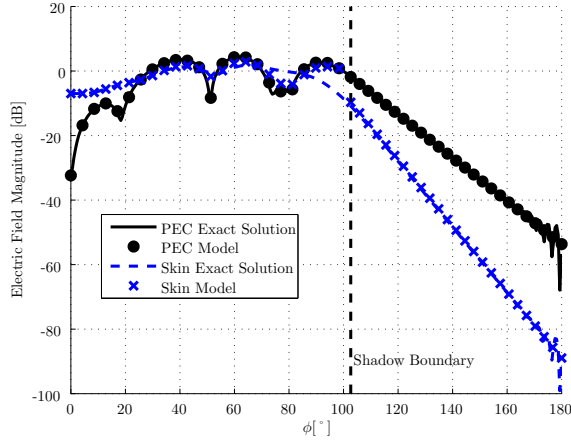


Fig. 6. TE mode. Comparison between the exact solution for a dielectric cylinder eq. (17), a PEC cylinder eq. (18) and the model with $f = 60$ GHz, $a = 0.2$ m and $\rho = 0.205$ m.

perfect fitting. It validates the first creeping wave mode is predominant at 60 GHz. The fact that influence of the creeping wave mode coming from the other side of the cylinder ($\phi < 0$) can be observed with the exact solutions around $\phi = 180^\circ$ where an interference pattern appears. Given the power level reached for those values of ϕ , it can be inferred that this creeping wave mode is negligible.

IV. EXPERIMENTAL COMPARISON

To assess the validity of the proposed model, two measurement campaigns have been conducted. The first one has been realized using a perfectly conducting (PEC) cylinder in order to precisely verify the theoretical path gain. The second campaign has been conducted on a human. Its purpose was to evaluate the validity of the model to emulate a real body though it has been developed for a cylinder.

A. PEC Measurement Campaign

The first experimental campaign has been done on a convex perfectly conducting cylinder (PEC). This campaign allows having a very accurate measurement of the path gain around the cylinder and validating precisely the creeping wave model.

1) *Experimental set-up*: The experimental geometry and the measurement set-up are presented in Fig. 7 and 8. The theoretical path gain has been verified by conducting measurements using an *Agilent E8361C VNA* in an anechoic chamber. U-band horn antennas were used with a beamwidth of 10° and a gain of 20 dB. The horn antennas have an aperture size of 3 cm x 2.3 cm.

As can be observed in Fig. 7, the Tx horn antenna is located far from the cylinder to obtain a plane wave illumination. The Rx horn antenna is located tangentially to the cylinder to maximize the amount of power received from the creeping wave. The distance Δr is defined from the middle of the horn antenna and δr defines the distance between the cylinder and

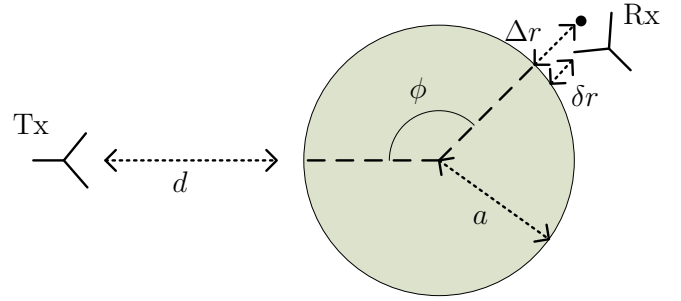


Fig. 7. Experimental Geometry. The receiving horn antenna (Rx) is located against the cylinder and $\Delta r = \rho - a$ is defined from the cylinder surface to middle of the horn antenna. δr defines the distance between the cylinder surface and the antenna's edge. The distance d is defined from the cylinder surface to the transmitting horn antenna (Tx).

TABLE II
SPATIAL PARAMETERS VALUES

Symbol	Value
a	0.2 m
d	1.92 m
ϕ	from 90° to 180°
Angular Step $\Delta\phi$	5° (or 10°)

the antenna. The parameters are summarized in Table II.

The cylinder has a height of 1.2 m and the horn antennas are placed at middle height. To discriminate the time of arrival of the creeping wave between two spatial positions with $\Delta\phi = 10^\circ$, a 10 GHz bandwidth is selected.

TABLE III
VNA FREQUENCY PARAMETERS VALUES

Symbol	Value
f_{start}	50 GHz
f_{stop}	60 GHz
f_{step}	66.67 MHz
VNA IFbandwidth	1 Hz
VNA Averaging parameter	1024

The frequency step is chosen in such a way that the length of the signal impulse response is $0.015 \mu\text{s}$ which is equivalent to a propagation length of 4.5 m is sufficient to discriminate the relevant paths. The IFbandwidth and the averaging parameter are chosen to get the highest dynamic range possible.

The bandwidth has been chosen between 50 GHz and 60 GHz. The upper frequency was limited because of the U-band (40 to 60 GHz) material available. The 10 GHz bandwidth was used to perform time-gating to increase the dynamic range. Time-gating will give the measured path gain in the center of the bandwidth : 55 GHz. For a 0.2 m radius PEC cylinder, the difference between the path gains at 55 GHz and 60 GHz is about 0.126 dB/cm for TM mode

and 0.055 dB/cm for TE mode (These values are calculated by using the theoretical equations of the path gain factors).

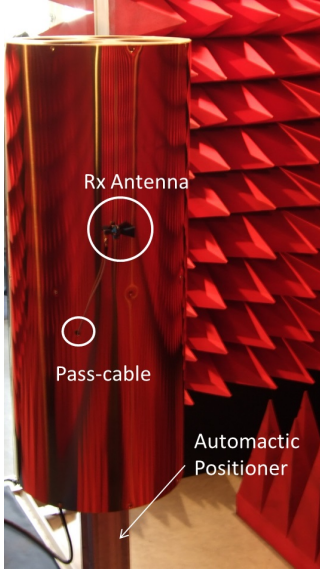


Fig. 8. Experimental Set-up.

The antenna was fixed on the cylinder. The whole cylinder was rotated thanks to an automatic angular positioner (*Newport MICRO-CONTROLE Motorized Rotation Stage RV Series*). The coaxial cables have about 6 dB/m losses. To avoid the need of long distance cables and optimize the received power, the VNA was put inside the anechoic chamber and covered by absorbing material. To minimize the cables movement during rotation, all the cables were passed inside the cylinder by a pass-cable expressly designed for.

This measurement campaign was conducted in order to validate the angular dependence of (30) and (40). Due to the use of horn antennas, the received field is integrated over the aperture size and so over ρ . These equations are separated variables solutions in terms of radial and angular variations. The integration over the aperture size does not change the angular variation. For the first values of ϕ around 90° , part of the horn antenna will be in the lit zone and the other in shadow one. The validity of the first measurements will be discussed in the following. To determine the shadow boundary influence, the receiving horn antenna is placed at two distances between the cylinder and the antenna $\delta r = 0$ mm (against the cylinder) and 20 mm. The second distance allows to have the entire aperture of the horn antenna in the lit region for the first measurement points. The distances Δr are summarized in Table IV by taking into account the antenna size for TM and TE modes.

2) Experimental Path Gains:

a) *Antenna against the cylinder:* The measurements made with the VNA are compared with (30) and (40) with the antenna against the cylinder ($\delta r = 0$). Fig. 9 is drawn by normalizing the theoretical path gains with respect to the measured received power at $\phi = 90^\circ$.

TABLE IV
DISTANCES BETWEEN THE CYLINDER AND THE RECEIVING HORN ANTENNA

Mode	δr [mm]	Δr [mm]
TM	0	15
	20	35
TE	0	11.5
	20	31.5

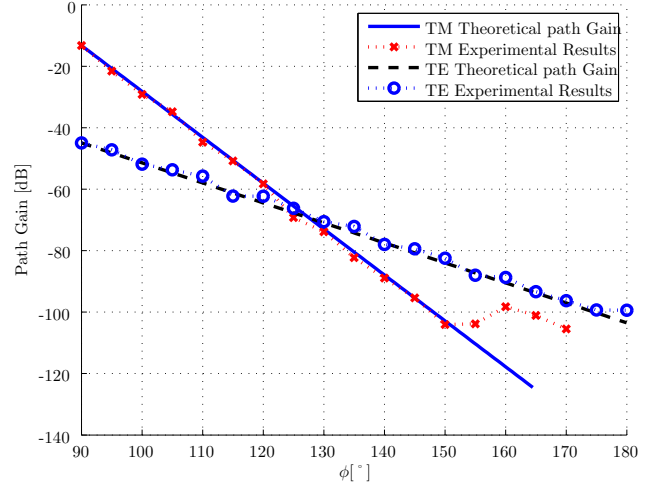


Fig. 9. PEC case, antenna against the cylinder. Comparison between the theoretical path gain and the measurements for TE and TM modes with $f = 55$ GHz.

As can be observed in Fig. 9, the model fits the measurements although after $\phi = 150^\circ$ the noise floor is reached and the measurements are no longer valid for TM case.

For TE propagation mode, only the ρ polarization of the electric field was measured because of the horn antenna position. Equation (40) is still valid noting that $E_\phi^{\text{TE}} \ll E_\rho^{\text{TE}}$ in the shadow zone. It can be seen that the dynamic range is higher due to the lower attenuation.

In these two results, measurements also fit for values around $\phi = 90^\circ$. The influence of the shadow boundary cannot be interpreted in those figures.

b) *Antenna at 2 cm away from the cylinder:* Path gain formulas are compared for the horn antenna at 2 cm from the cylinder which is equivalent to $\Delta r = 35$ mm (TM) and $\Delta r = 31$ mm (TE).

In Fig. 10, it can be seen that measurements deviate from the path gain model below $\phi = 110^\circ$. The shadow boundary has been outlined for a better understanding. In this figure, unlike Fig. 9, the shadow boundary influence is clearly visible due to the fact that the entire receiving antenna was in the lit zone at the beginning of the measurements. These measurement positions should have been modeled with GO.

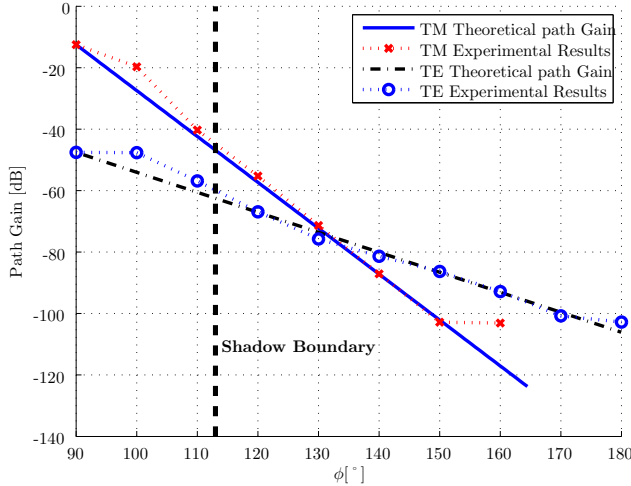


Fig. 10. PEC case, antenna at 20 mm of the cylinder. Comparison between the theoretical path gain and the measurements for TE and TM modes with $f = 55$ GHz.

TABLE V
MAIN TIME-FREQUENCY PARAMETERS

Symbol	Value
f_0	60 GHz
VNA IFbandwidth	1 Hz
VNA Averaging parameter	1024
Measurement duration	60 s
Time averaging snapshots	48

B. Real Human Measurement Campaign

The second set of experiments was conducted on a real human body. The human body is compared with a dielectric ($\epsilon'_r = 7.9753$ and $\sigma = 36.397$ S/m [11]) cylinder having with the same perimeter.

1) *Experimental set-up*: The experimental set-up used for this campaign is the same as the one presented in Fig. 8. The measurements were done at a single frequency $f_0 = 60$ GHz, to have quicker measurements. Each measurement was carried out during 60 seconds to average the influence of the small movements of the body. This measurement time is equivalent to 48 snapshots per spatial position. The main parameters of this campaign are presented in Table V.

The experiments were done around a human torso of 93 cm of perimeter. It is equivalent to a cylindrical body with a radius of about 14.8 cm. A spatial step of 1.5 cm was chosen which is equivalent to an angular step of 5.8° . These parameters are summarized in Table VI.

The arms of the body remained up not to disturb the measurement around the torso.

2) *Experimental Path Gains*: The theoretical gain factors for a cylinder with different values of radius a [cm] are summarized in Table VII.

Measurement results for the TM polarization are shown in

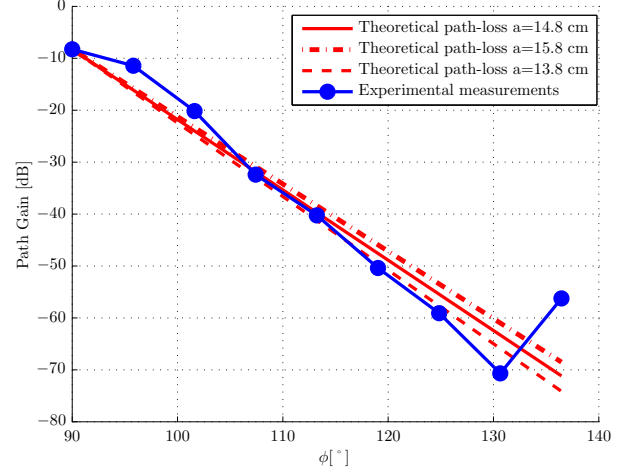


Fig. 11. Human case. TM mode. Antenna against the body. Comparison between the TM theoretical path gain for different radius a with $\Delta r = 15$ mm at $f = 60$ GHz.

Fig. 11. The mean value of the received power fits the theoretical path gain (normalized according to the first experimental value). Measurements have been conducted up to 140° . Beyond that angle, the main path reaches the measurement noise level. Time gating could not be performed because of the single-frequency measurement constraint.

The TE case is shown in Fig. 12. Measurements have been done in a larger range than the TM case because of the higher dynamic range. Experiment and theoretical results show a good agreement as well.

These results show the validity of using a simple path gain formula obtained with an equivalent cylinder for a real body. As can be observed, different theoretical curves have been plotted to study the sensitivity of the radius a of the equivalent cylinder, by choosing a maximum error of 1 cm. It can be observed in Table VII that an error of 5% on a gives an error of 3.5% on $n_{\text{skin}}^{\text{TM}}$ and 2.75% on $n_{\text{skin}}^{\text{TE}}$. Fig. 11 and 12 show that these differences are negligible. Evaluation of the standard deviation (STD) has been done in [dB] to compare the cylindrical model and the measurements. The errors are summarized in Table VIII.

This table shows that the STD hardly changes with the equivalent radius a . The low sensitivity of the theoretical path

TABLE VI
MAIN SPATIAL PARAMETERS

Symbol	Value
Body Perimeter	93 cm
Equivalent Radius	14.8 cm
Spatial step	1.5 cm
Angular step	5.8°
d	1.92 m

TABLE VII
THEORETICAL PATH GAIN FACTORS

a [cm]	$n_{\text{skin}}^{\text{TM}}$ [dB/cm]	$n_{\text{skin}}^{\text{TE}}$ [dB/cm]
13.8	5.489	3.552
14.8	5.242	3.426
15.8	5.021	3.304

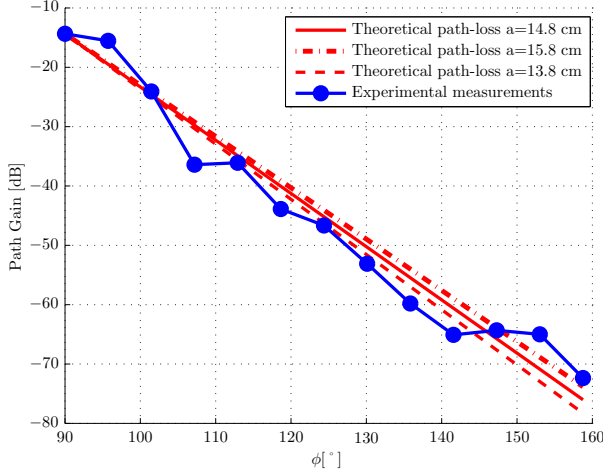


Fig. 12. Human case. TE mode. Antenna against the body. Comparison between the TE theoretical path gain for different radius a with $\Delta r = 11.5$ mm with $f = 60$ GHz.

TABLE VIII
STANDARD DEVIATION WITH THE EQUIVALENT RADIUS

a [cm]	STD _{TM} [dB]	STD _{TE} [dB]
13.8	3.77	3.69
14.8	3.69	3.67
15.8	5.12	3.76
Minimum STD		
14.4	3.57	-
14.9	-	3.66

gain curve allows an error of 1 cm on the radius a .

V. CONCLUSIONS

This paper investigates an off-body diffraction model at 60 GHz around dielectric and PEC cylinders modeling the human body. The propagation model is developed for both TM and TE polarizations. The model assumes that the propagation can be described by geometrical optics in the lit region and by a creeping wave in the shadow one. By using Watson's transformation, the TM and TE creeping waves are deduced from the boundary problem of the plane wave scattering by a cylinder.

Numerical simulations have been done to validate the model. The PEC solution has also been compared to the

dielectric cylinder with the properties of the human skin at 60 GHz. It has been observed that the propagation around a PEC cylinder is an excellent approximation of the propagation around a dielectric one only for TM polarization. For TE polarization, it has been shown that the ρ component dominates the ϕ one in the shadow region.

The experimental validation has been done on a PEC cylinder for both polarizations. The creeping wave path gains perfectly fits with the theoretical propagation model developed in this paper.

A second experimental campaign with a real body has been done to validate the theoretical path gains in the dielectric case. The measurements show excellent agreement with the theory. These experimental results prove that the propagation model is accurate and is thereby well suited for being included in a standard such as IEEE 802.11ad.

One limitation of the model is its simplified geometry. A model based on a more realistic geometry such as an elliptic cylinder should give more accurate results. The model is also limited to normal incidence. The elevation angle should be taken into account in future works.

REFERENCES

- [1] M. Abramowitz and I. A. Stegun. *Handbook of Mathematical Functions with Formulas, Graphs, and Mathematical Tables*. 1992: Dover.
- [2] S. Alipour, F. Parvaresh, H. Ghajari, and D. F. Kimball. Propagation characteristics for a 60 GHz wireless body area network (WBAN). *Proc. Military Commun. Conf.*, pages 719–723, 2010.
- [3] W. C. Chew. *Waves and Fields in Inhomogeneous Media*. New York: IEEE Press, 1995.
- [4] S. L. Cotton, W. G. Scanlon, and P. S. Hall. A simulated study of co-channel inter-ban interference at 2.45 GHz and 60 GHz. *Proc. Eur. Wire. Techn. Conf.*, pages 61–64, 2010.
- [5] A. Fort, C. Desset, P. De Doncker, P. Wambacq, and L. Van Biesen. An ultra-wideband body area propagation channel model—from statistics to implementation. *IEEE Trans. Microw. Theory Tech.*, 54:1820–1826, 2006.
- [6] A. Fort, F. Keshmiri, G. R. Crusats, C. Craeye, and C. Oestges. A body area propagation model derived from fundamental principles: Analytical analysis and comparison with measurements. *IEEE Trans. Antennas Propag.*, 58(2):503–514, 2010.
- [7] A. Fort, J. Ryckaert, C. Desset, P. De Doncker, P. Wambacq, and L. Van Biessen. Ultra-wideband channel model for communication around the human body. *IEEE J. Sel. Areas Commun.*, 24(4):927–933, 2006.
- [8] N. Guo, R. C. Qiu, S. Mo, and K. Takahashi. 60-GHz millimeter-wave radio: Principle, technology, and new results. *EURASIP J. Wireless Commun. Netw.*, 2007, 2007.
- [9] C. Gustafson and F. Tufvesson. Characterization of 60 GHz shadowing by human bodies and simple phantoms. *Proc. 6th Eur. Conf. Antennas Propag.*, 2012.
- [10] P. S. Hall and Y. Hao. *Antennas and Propagation for Body-Centric Wireless Communications*. Artech House, 2006.
- [11] P. A. Hasegall, E. Neufeld, M.-C. Gosselin, A. Klingenböck, and N. Kuster. IT'IS database for thermal and electromagnetic parameters of biological tissues, version 2.2. July 11th, 2012.
- [12] V. I. Ivanov. Tabulation of the functions of VA fock. *J. Math. Sci.*, 19(4):1355–1365, 1982.
- [13] A. Khafaji, R. Saadane, J. El Abbadi, and M. Belkasm. Ray tracing technique based 60 GHz band propagation modelling and influence of people shadowing. *International Journal of Electrical, Computer, and Systems Engineering*, 2(2):102–108, 2008.
- [14] Y. A. Kravtsov and N. Y. Zhu. *Theory of Diffraction : Heuristic Approaches*. 2010: Alpha Science.
- [15] L. D. Landau and E. M. Lifshitz. *Electrodynamics of Continuous Media*. 1984: Pergamon.

- [16] A. Maltsev et al. 60 GHz WLAN experimental investigations. *IEEE 802.11 TGad document: IEEE doc. 802.11-08/1044r0*, 2008.
- [17] A. Maltsev et al. Channel modeling for 60 GHz WLAN systems. *IEEE 802.11 TGad document: IEEE doc. 802.11-08/0811r1*, 2008.
- [18] A. Maltsev et al. Channel models for 60 GHz WLAN systems. *IEEE 802.11 TGad document: IEEE 802.11-09/0334r8*, 2010.
- [19] T. Mavridis, L. Petrillo, J. Sarrazin, D. Lautru, A. Benlarbi-delaï, and P. De Doncker. Analytical creeping waves model at 60 GHz for off-body communications. *Eucap2013*, pages 574–578, Apr. 2013.
- [20] P. H. Pathak, W. D. Burnside, and R. J. Marhefka. A uniform GTD analysis of the diffraction of electromagnetic waves by a smooth convex surface. *IEEE Trans. Antennas Propag.*, AP-28(5):631–642, 1980.
- [21] J. Ryckaert, P. De Doncker, R. Meys, A. de le Hoye, and S. Donnay. Channel model for wireless communication around human body. *Electron. Lett.*, 40(9):543–544, 2006.
- [22] H. H. Syed and J. L. Volakis. High frequency scattering by a smooth coated cylinder simulated with generalized impedance boundary conditions. *Radio Sci.*, 26:1305–1314, 1991.
- [23] C. A. Valagiannopoulos. An overview of the watson transformation presented through a simple example. *Progress In Electromagnetics Research, PIER 75*, pages 137–152, 2007.
- [24] S. Van Roy, C. Oestges, F. Horlin, and P. De Doncker. On-body propagation velocity estimation using ultra-wideband frequency-domain spatial correlation analyses. *Electron. Lett.*, 43(25):1405–1406, 2007.
- [25] S. K. Yong and C. C. Chong. An overview of multigigabit wireless through millimeter wave technology: Potentials and technical challenges. *EURASIP J. Wireless Commun. Netw.*, 2007:10 pages, 2006.
- [26] Y. Zhao, Y. Hao, A. Alomainy, and C. G. Parini. UWB on-body radio channel modeling using ray theory and subband FDTD method. *IEEE Trans. Microw. Theory Techn.*, 54:1827–1835, 2006.